Leading-Edge Vortex Structure of Nonslender Delta Wings at Low Reynolds Number

Michael V. Ol*

U.S. Air Force Research Laboratory, Wright–Patterson Air Force Base, Ohio 45433-7542

and

Morteza Gharib[†]

California Institute of Technology, Pasadena, California 91125

The velocity field near the apex region of moderately swept delta wings was measured in a water tunnel, using a version of stereoscopic digital particle imaging velocimetry. Flow visualization was also used to verify these results. In contrast to most recent studies, low angles of attack were emphasized, with most data in the range of 5–20 deg. Delta wings of 50- and 65-deg leading-edge sweep and 30-deg windward-side bevels were tested at Reynolds numbers of 6×10^3–1.5×10^4. At these low Reynolds numbers, secondary leading-edge vortices were weak, giving way to essentially stagnant flow outboard of the primary leading-edge vortices at the higher angles of attack. Otherwise, velocity data for the 65-deg wing were consistent with well-known observations for slender delta wings. The 50-deg wing exhibited unexpectedly strong primary leading-edge vortices at low angles of attack, with a generally conical velocity field. Upstream progression of vortex breakdown with increasing angle of attack exhibited extensive regions of streamwise undulation. Leading-edge shear-layer rollup was observed in crossflow planes well downstream of the breakdown region, but with an increased occurrence of paired vortical structures of opposite sign inside the shear layer itself.

Nomenclature

b	=	wingspan at a given streamwise station
c	=	wing root chord
U_x, U_θ	=	axial and azimuthal velocity components at a given streamwise station
U_∞	=	freestream velocity
u, v	=	Cartesian velocity components at a given streamwise station
x, y, z	=	Streamwise, spanwise, and vertical coordinates, respectively
α	=	wing geometric angle of attack
Γ	=	circulation
Λ	=	wing leading-edge sweep angle
ϕ	=	lens-to-camera angle in rotational-type stereoscopic velocimetry
ω_x	=	streamwise component of vorticity

I. Introduction

DELTA wings have found application for several decades in maneuvering combat aircraft and supersonic aircraft. In both cases, these wings are generally of large sweep in an effort to reduce supersonic wave drag.[1] Lower-sweep wings used in fighter aircraft are generally accompanied by high-sweep strakes.[2] A pure delta wing of small sweep, however, is rarely encountered. One reason for this is doubt regarding the stable and manageable presence of the leading-edge vortices (LEVs) generated by such wings that are so critical to delta wing performance.[3]

The stall behavior of classical high-aspect-ratio wings and the breakdown of the LEVs of slender delta wings are an extensively investigated problem, especially for steady-state conditions. However, the transitional case, that of the delta wing of relatively high aspect ratio, has not been as widely studied. Questions remain, for example, as to what extent the downstream development of the velocity field follows the conical pattern cited in calculations[4] and experiments[5] for slender wings, namely, whether a stable LEV system is even sustainable for a delta wing of moderate sweep at any angle of attack and, if the LEVs do exist, how they encounter vortex breakdown. Typically, with increasing angle of attack, it is the upstream progression of breakdown toward the wing apex that results in a stall-type situation for a slender delta wing. This process can occur in various forms and to various extents of unsteadiness.[6] Because the angle of attack at which the LEVs of a slender wing burst is quite high, interaction of the primary LEVs and near-surface phenomena, such as the secondary vortices and the leeward-side boundary layer, is limited.[7] Hummel[5] points out that the interaction between primary and secondary vortices is dependent on whether the leeward boundary layer is laminar or turbulent. In the laminar case, the secondary vortices tend to displace the primary vortices farther inboard and above the leeward surface of the wing.

For a 60-deg wing, Shih and Ding[7] have identified the importance of the secondary LEV in affecting the primary LEV and, in particular, in interacting with identifiable vortical structures within the leading-edge shear layer. Indeed, there has been considerable recent interest in the role of such structures. At the low incidence angles involved, the LEVs are close to the wing surface, and vortex breakdown regions interact strongly with flow near the leeward surface. The present study extends these results to the 50-deg wing.

Because breakdown occurs at lower angle of attack for wings of progressively lower sweep, it stands to reason that the interaction of the LEVs and of their breakdown process with the leeward boundary layer should increase with decreasing sweep. This progression should ultimately culminate in a stall process at angles of attack comparable to those for conventional high-aspect-ratio wings. However, few previous experiments have reported such conditions, either because data for delta wing investigations were concerned with the more usual higher angles of attack (for example, Ref. 8), higher leading-edge sweep (Payne et al.[9]), or because the LEV was observed to progress toward the wing apex and a stable vortex pair was not present. Wentz and Kohlman[10] considered a wing of 50-deg sweep, but their data set begins at $\alpha = 15$ deg. Nelson and Pelletier[11] took flow visualization data for a 50-deg wing at $Re = 5 \times 10^4$ for

*Aerospace Engineer, Air Vehicles Directorate, Aeronautical Sciences Division 2130 8th Street, Building 45. Member AIAA.

†Professor of Aeronautics, Graduate Aeronautical Laboratory, Mail Code 205-45, 1200 East California Boulevard. Senior Member AIAA.
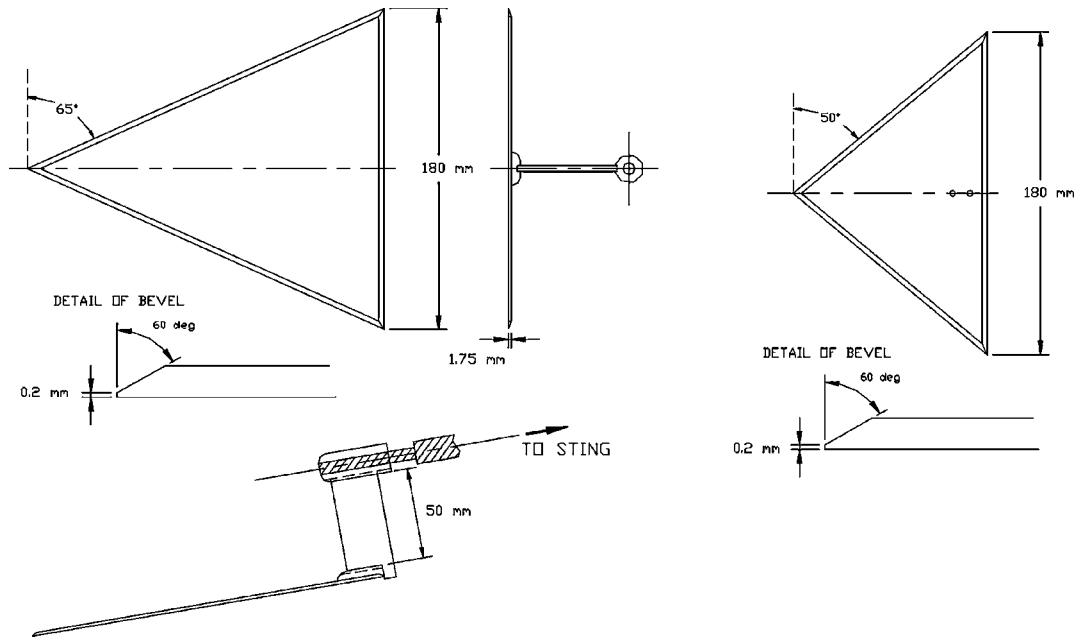
Fig. 1 Λ = 65- and 50-deg delta wing models, with mounting arrangement.

angles of attack from 7 to 18 deg. At 7 deg, breakdown was observed to lie at approximately $x/c = 0.75$ and reached the apex by 18 deg, evidently without appreciable unsteadiness. The data of Honken and Andreopoulos[12] and the classical experiment of Earnshaw and Lawford[13] suggest that, for a delta wing of 45-deg sweep angle, flow over the leeward side is in a postbreakdown state at all angles of attack where leading-edge separation was observed. Miau et al.[14] observed that dependency of the LEV behavior on the leading-edge shape of a 50-deg wing is stronger than what might have been expected from results for more slender wings.[15]

This paper describes an experimental investigation of the structure and decay of the LEVs produced by a nonslender delta wing, that is, a wing of moderate sweep. In particular, a wing of 50-deg leading-edge sweep (aspect ratio 3.36) is studied. The 50-deg wing is compared to a 65-deg wing of similar geometry. Experiments were conducted in a water tunnel. The Reynolds number based on root chord was 8.5×10^3 for the 50-deg wing and 1.54×10^4 for the 65-deg wing.

Three-component velocity field data assist in understanding the complex flow structures. The question is how to obtain such data. The principal experimental technique used in the present experiment is that of stereoscopic digital particle image velocimetry (SPIV). A "rotational" arrangement of SPIV[16] is adapted to the environment of a water tunnel. Video-based image sequences are taken in planar cuts normal to the freestream, passing through the wing model and, in particular, focusing on the starboard primary and secondary LEV region. As a result, all three components of velocity are obtained over a sequence of planar domains, tracking the trajectory of the primary LEV core, as well as producing a snapshot of the flowfield over the leeward surface of the wing. These velocity data can then be used to elucidate the presence of coherent vortical structures and to assess how the decay of these structures with increasing angle of attack can be interpreted as a passage toward stall of the wing. Qualitative discrepancies with known results for the baseline 65-deg wing are attributed to viscous effects that become important at low Reynolds number.

II. Experimental Setup

A. Facility and Models

Experiments were conducted in a low-speed free-surface water tunnel, primarily at a test section flow speed of 80 mm/s. The tunnel, built in conjunction with this experiment, has a test section width of 45 cm and height of 60 cm. The facility is described in detail in Refs. 17 and 18.

Two delta wings models were used, with leading-edge sweeps of 50 and 65 deg. The latter model represents a configuration heav-
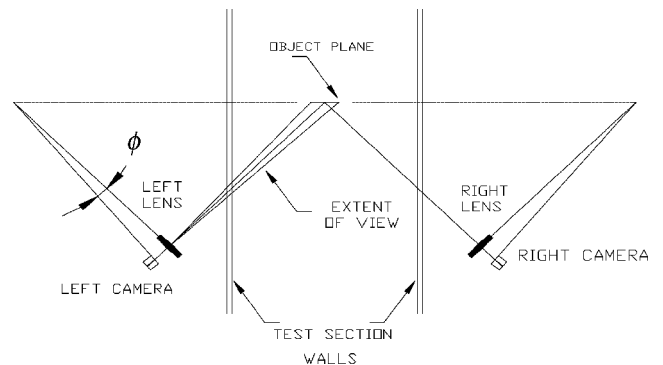

Fig. 2 Camera and lens arrangements for SPIV, top view.

ily studied in recent times[19] and was used as a baseline proof of concept. The former was taken as a prototypical nonslender wing. Both models had 180-mm trailing-edge spans and 30-deg windward side bevels and were machined from 3.17-mm (0.125-in.) thick Plexiglas®. The two delta wing models and their mounting arrangement are shown in Fig. 1.

B. SPIV Setup

The SPIV setup used in the present study is based on the two-dimensional digital particle image velocimetry (PIV) technique of Willert and Gharib,[20] normally implemented with one camera. In the present case, two charge-coupled device (CCD) digital video cameras are focused onto the region of interest, located in the interrogation plane. In the rotational version of SPIV applied here, the two cameras view the interrogation plane off-axis, with each camera rotated at some angle relative to the interrogation plane. This results in an apparent variation of magnification across the field of view of each camera. In-plane velocities recorded by the two cameras are combined by simple trigonometric relations to yield all three components of velocity, with comparable accuracy in all three directions.[21] The camera CCD planes are rotated with respect to their objective lenses according to the Scheimpflug criterion (Fig. 2), with the lens-to-camera angle ϕ selected such that the entire field of view is in focus, even for large lens aperture settings.[16] Perspective distortion effects are removed by means of a calibration procedure, wherein one takes tare images of a single Cartesian grid. Images of rectangles are registered as trapezoids by the two cameras. An inverse mapping that "dewarps" trapezoids back into rectangles is applied to the raw images of the PIV tracker particles before the PIV image

processing. This mapping also removes left–right camera misalignment and attempts to correct for spherical distortion in the camera lenses.

The off-axis orientation of the cameras results in problems of light refraction in going from the water-tunnel test section, through the glass walls of the test section, and then to the cameras placed outside the test section. This was circumvented by placing mirrors in the test section, approximately four wingspans downstream of the

Fig. 3   Stereo PIV arrangement in water tunnel.

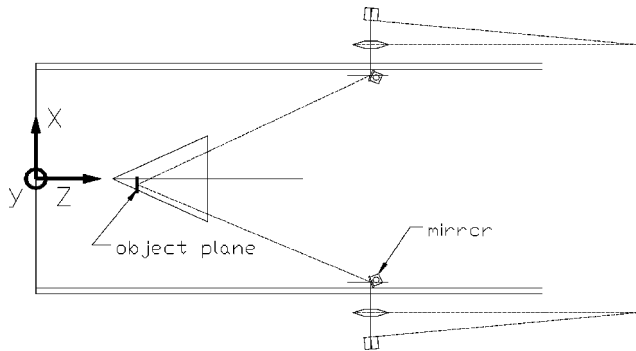

Fig. 4   Arrangement of SPIV interrogation planes.

delta wing models. The mirrors reflect images of the interrogation domain before passing to the lenses and cameras, such that the light passes normal to the test section walls. The resulting setup amounts to a "folded" Scheimpflug arrangement, as shown in Fig. 3.

SPIV data were taken in succeeding crossflow planes over the starboard panel of the wing, near the apex region. The physical size of the interrogation domain was 33.2×24.9 mm, imaged by CCD cameras of 640×480 pixels. The scheduling of the interrogation planes for the two wings is shown in Fig. 4.

A double-pulsed 50-mJ frequency-doubled Nd:YAG laser, firing at an effective rate of 30 Hz, was used to produce a light sheet for the SPIV. The light sheet was place normal to the freestream flow direction and was stepped downstream within each pair of pulses to increase the frame-to-frame tracker particle correlation as the particles convected with the flow normal to the light sheet. Rhodamine-coated particles of 0.92–1.1 specific gravity and $\sim$20–40 μm diam were used[22] as tracker particles. The arrangement of the light sheet, cameras and lenses, and models in the test section is shown in Fig. 5.

C.   Error Estimations

The techniques just outlined resulted in systematic optical errors in addition to the usual measurement and signal processing errors associated with two-dimensional digital PIV. The former can to some extent be quantified by considering, for example, a measurement of the tunnel freestream velocity field, in a region coincident with measurements of the delta wing flowfield data. Figure 6 shows a streamwise view, with the freestream direction normal to the page. A uniform flow would, of course, have zero in-plane velocity and uniform out-of plane velocity. Figure 6 is the result of averaging 100 image pairs over 6.7 s. In both Figs. 6a and 6b, the eventual typical location of the delta wing is superimposed over the field of view. Figure 6a shows contours of measured in-plane velocity error, defined here as the magnitude of in-plane velocity components normalized by the freestream out-of-plane velocity, computed at each data point in the interrogation domain by $E \equiv \sqrt{(u^2 + v^2)}/U_\infty$. Freestream velocity was independently measured by one-component laser-Doppler velocimetry and also by a simple propeller meter. Values of E in the region of interest are on the order of 3–5% of the freestream velocity. Figure 6b shows contours of out-of-plane velocity. The measured out-of-plane velocity is biased by values of from −5% to +2%, in going along the spanwise direction of the interrogation domain. The
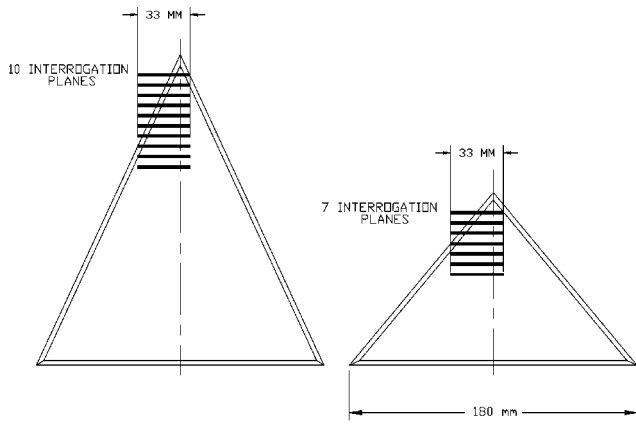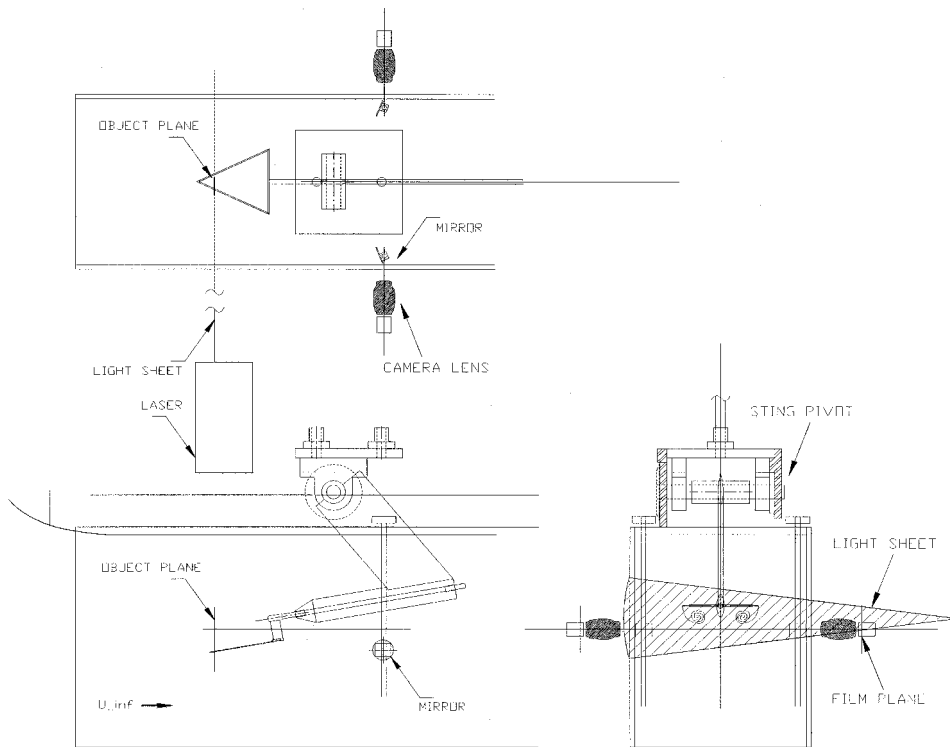
Fig. 5   Three-view drawing of test section, model mounting, and optics.

cause of these systematic errors can be attributed to the image de-warping technique, which relies on a single calibration plane. This essentially attempts to map spatial regions into planar regions. A more rigorous (but more complex) multiplane calibration would allow a better reconstruction of the mapping of a three-dimensional domain into a planar domain.[23] In the following, averaged velocity data at any point in the interrogation domain can be considered to have an error bounded by, for example, 10%. This error range is acceptable for the qualitative conclusions.

Spatial discretization error is essentially the same as for the two-dimensional DPIV technique. There were 32×32 pixel windows with 8×8 pixel shifting used, with a physical domain 24.8×33 mm in extent. With similar settings for grid turbulence experiment, Westerweel et al.[24] report a 0.04 pixels rms displacement error for a representative PIV seeding particle size, which translates under present conditions to 0.5% of freestream velocity. A flow structure with characteristic length of less than half of a PIV window size will not be resolved adequately due to spatial averaging. This translates to 0.4 mm or 1.6% of the local semispan at the streamwise location of predominant interest, at $x/c = 0.296$. A comparable vortical structure of interest would be nominally 4% of the local semispan in characteristic length.
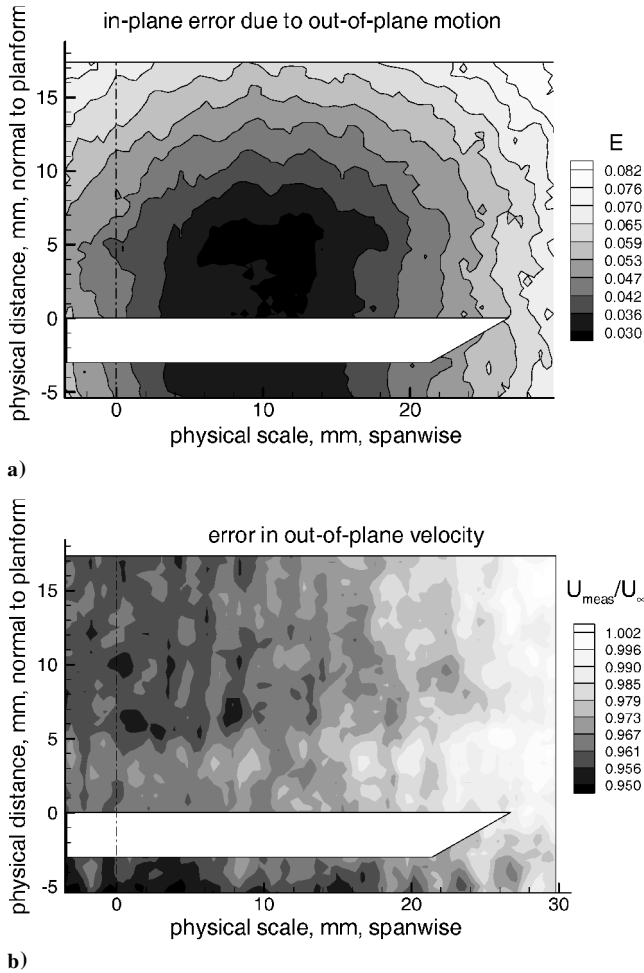
D. Flow Visualization

Flow visualization was conducted as a simple attempt to validate the SPIV data. Dye was injected in the standard manner, by means of a probe placed into the region of the windward stagnation point. As for the SPIV, two simultaneously triggered CCD video cameras recorded the dye injection events, making available a planform view and a side view.

III. Results

A. Flow Visualization

The dye injection revealed the presence of coherent LEVs for both the 65- and 50-deg wings, down to $\alpha = 2.5$ deg. Figure 7 illustrates the situation for the 50-deg wing at some representative angles of attack.

For the conditions of the present experiments, at angles of attack of 10 deg and below, the 50-deg wing developed strong LEVs, with breakdown no farther upstream than the midchord. This is rather different from some earlier results[14] for this sweep angle, although a partial explanation for the prevalence of coherent LEVs is based on the particular choice of leading-edge bevel geometry. Classical results, mostly at higher Reynolds number, also suggest that wings of such low sweep do not generate appreciable LEVs (Ref. 13, for example). At $\alpha = 20$ deg, organized streamwise vortical flow appears to have disintegrated and was replaced by "bubble" separation over the leeward surface. In the side view, this flow appears to be separated from the freestream by a shear layer, which itself exhibits Kelvin–Helmholz rollers. Whereas the flow bounded by this shear layer undulates without a discernable pattern, the location of the shear layer is relatively steady.

In going from the very steady, low angle of attack flow regime to the high angle of attack separated flow regime, the flowfield undergoes appreciable unsteadiness, as described in Ref. 25. The left and right vortex breakdown points were observed to undergo motions in the streamwise direction to an extent on the order of 0.4 root chords, in which the left and right vortices disintegrate and reform on a quasi-alternating basis. This occurred in the $\alpha = 12.5$–17.5 deg range.
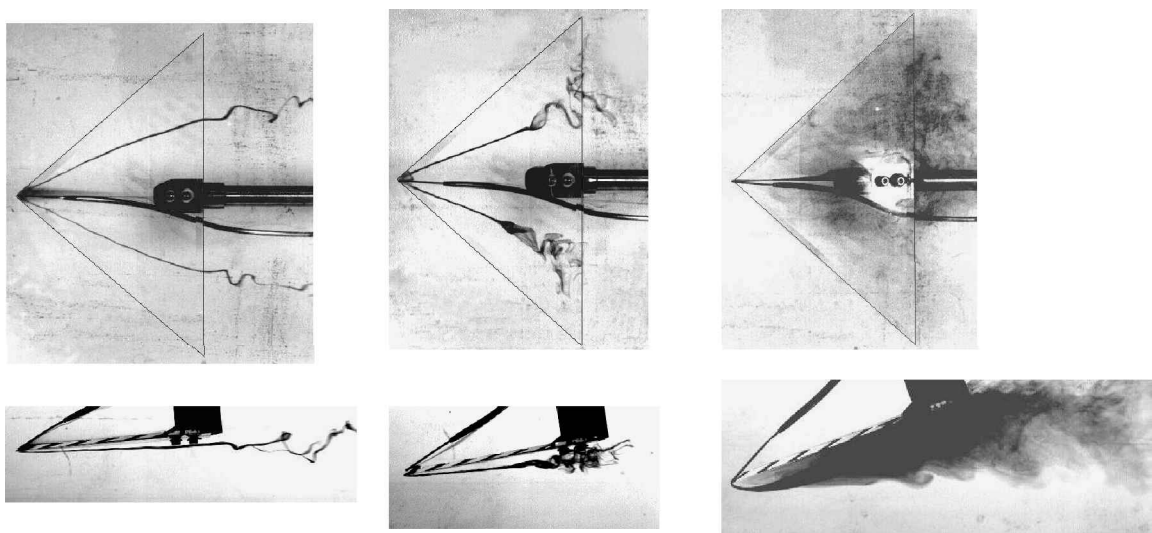

a)

b)

Fig. 6 Errors of mean measurement of freestream velocity.

Fig. 7 Dye streaks following primary LEVs for 50-deg wing: $\alpha = 5$, 10, and 20 deg; planform and side views.
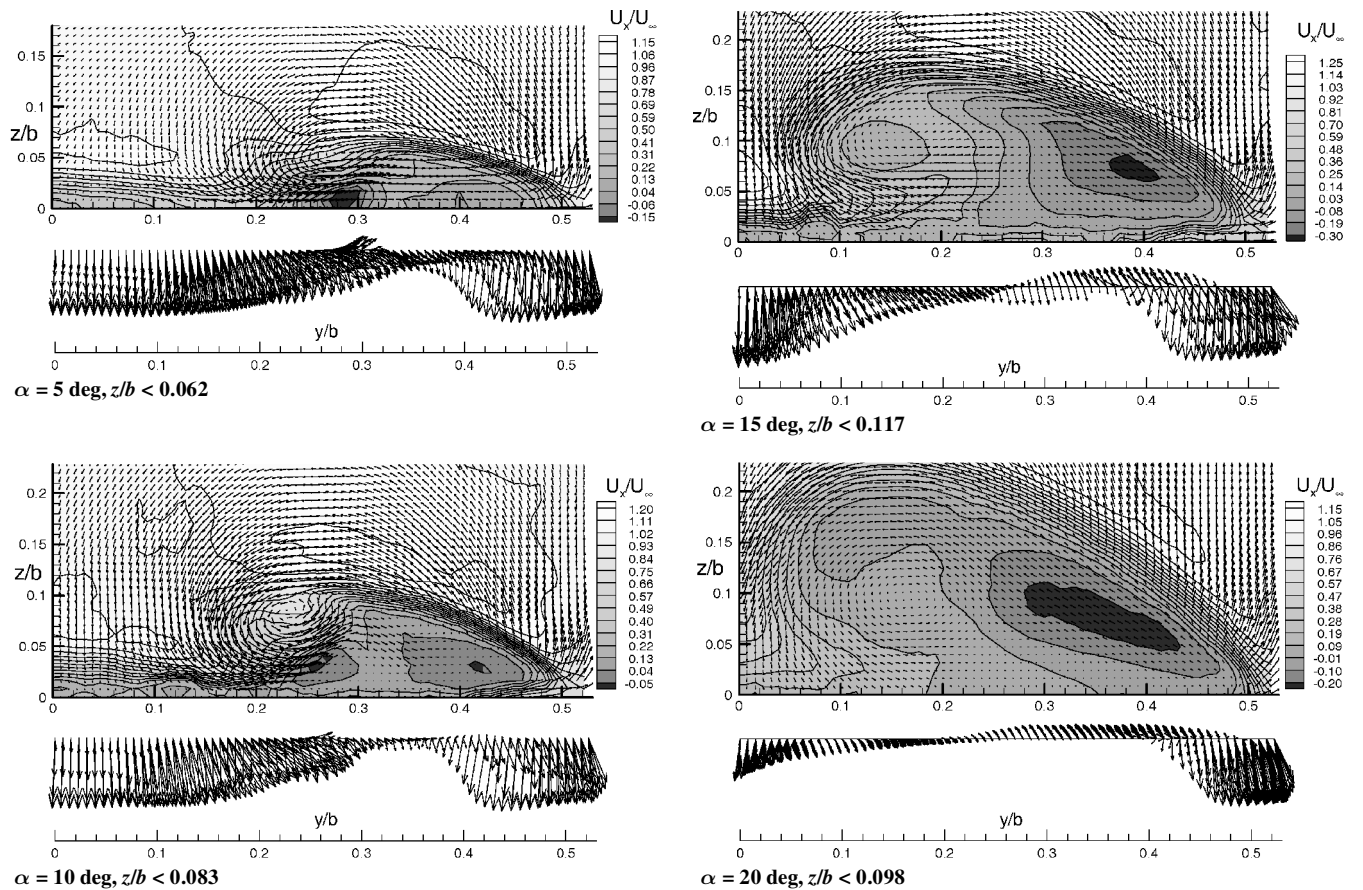
Fig. 8   Streamwise and planform views of the mean starboard flow pattern, 50-deg wing; *x/c* = 0.296; coordinates expressed in fractions of local span.

B.   SPIV

SPIV velocity vector plots are given for the $\Lambda = 50$ deg (Fig. 8) and $\Lambda = 65$ deg (Fig. 9) wings, at $\alpha = 5, 10, 15$, and 20 deg. More detailed mean and instantaneous data, including rms velocity data, are presented in Ref. 18. In an effort to illustrate three-component vector data on their two-dimensional domain, two views are given. The first is looking upstream at a region over the starboard semispan of the wing, referred to as the streamwise view. The wing centerline is at $y/b = 0$, where b is the wingspan at the given streamwise station. The second view is the planform view, edited to show only that portion of the interrogation domain that is at or below the z/b cut passing through the primary LEV core axis; this z/b value is given for each data set. The grayscale color bar legend indicates contours of out-of-plane velocity, normalized by the freestream value. Regions of lowest out-of-plane velocity are the darkest and are generally outboard and below the primary leading-edge vortex and inboard and below of the leading-edge shear layer. The flow visualization experiments showed that the sweep of the vortex core trajectories for both wings was quite small, on the order of 20 deg. The casual interchange of the terms "axial velocity" and "out-of-plane velocity" in the vicinity of the primary LEV core introduces an error of some 6%. This treatment is adopted here for convenience because the realignment of the SPIV interrogation planes to measure true axial velocity is prohibitively cumbersome. The velocity vector images are averages taken over 200 samples, which correspond to 2.8 and 5.0 convective times for the 65- and 50-deg wings, respectively.

Broadly speaking, the planform views of the velocity vector plots in Fig. 9 exhibit a weak "jetlike" LEV axial velocity profile, whereas those of Fig. 8 have a "wakelike" axial velocity profile. The latter is akin to that of a postbreakdown leading-edge vortex. This is not surprising for the $\alpha = 15$- and 20-deg cases because by then the breakdown location has crossed the SPIV interrogation plane. However, for the $\alpha \leq 10$-deg cases, breakdown is downstream of the interrogation plane. For the 50-deg wing, the leading-edge shear layer is well resolved even at $\alpha = 20$ deg. It maintains a rolled-up structure, despite that the flow bounded by the shear layer and the

wing leeward surface is strongly decelerated and that a discernable leading-edge vortex is missing. This situation was observed in all of the SPIV interrogation planes, from $x/c = 0.12$ to 0.3.

The time-averaged data presented in Figs. 8 and 9 differ marginally from instantaneous data, mostly in small-scale variations present in the latter, but attenuated in the former. However, the $\alpha = 12.5$- and 15-deg cases for the 50-deg wing have appreciable differences between mean and instantaneous results, as discussed in Ref. 25.

C.   Velocity Profiles
1.   Results at a Particular Streamwise Station

When cuts are taken along the appropriate distance above the leeward surface, velocity profiles can be constructed from the vector plots (Figs. 8 and 9) shown in the preceding section. Again, one has to contend with the issue of how to represent three-dimensional data. The natural choice is to cut through the primary vortex core. Figure 10 shows these data for the station $x/c = 0.296$ for both wings and six angles of attack. The origin is again at the wing center plane, and the local leading edge is at $y/b = 0.5$.

For the 65-deg wing, the LEV core axial velocity increases with respect to freestream velocity as the angle of attack is increased. By $\alpha = 20$ or even 15 deg, the familiar jetlike velocity profile can be observed. In fact, the peak axial velocity, as normalized by the freestream, increases roughly linearly with increasing angle of attack. The situation is quite different for the 50-deg wing.

For both wings, the region outboard of the primary LEV core area and inboard of the leading-edge (LE) shear layer exhibits decreasing axial velocity with increasing angle of attack, at some points even containing pockets of reversed flow. This has curious implications for the "breakdown" of the secondary LEV. In particular, one could surmise that, because this near-stagnant condition appears at angles of attack where the primary LEV is still coherent (10 deg for both wings), the secondary LEV breakdown precedes that of the primary LEV. For at least the Reynolds number and bevel geometry conditions of the present experiment, the behavior of the secondary LEV
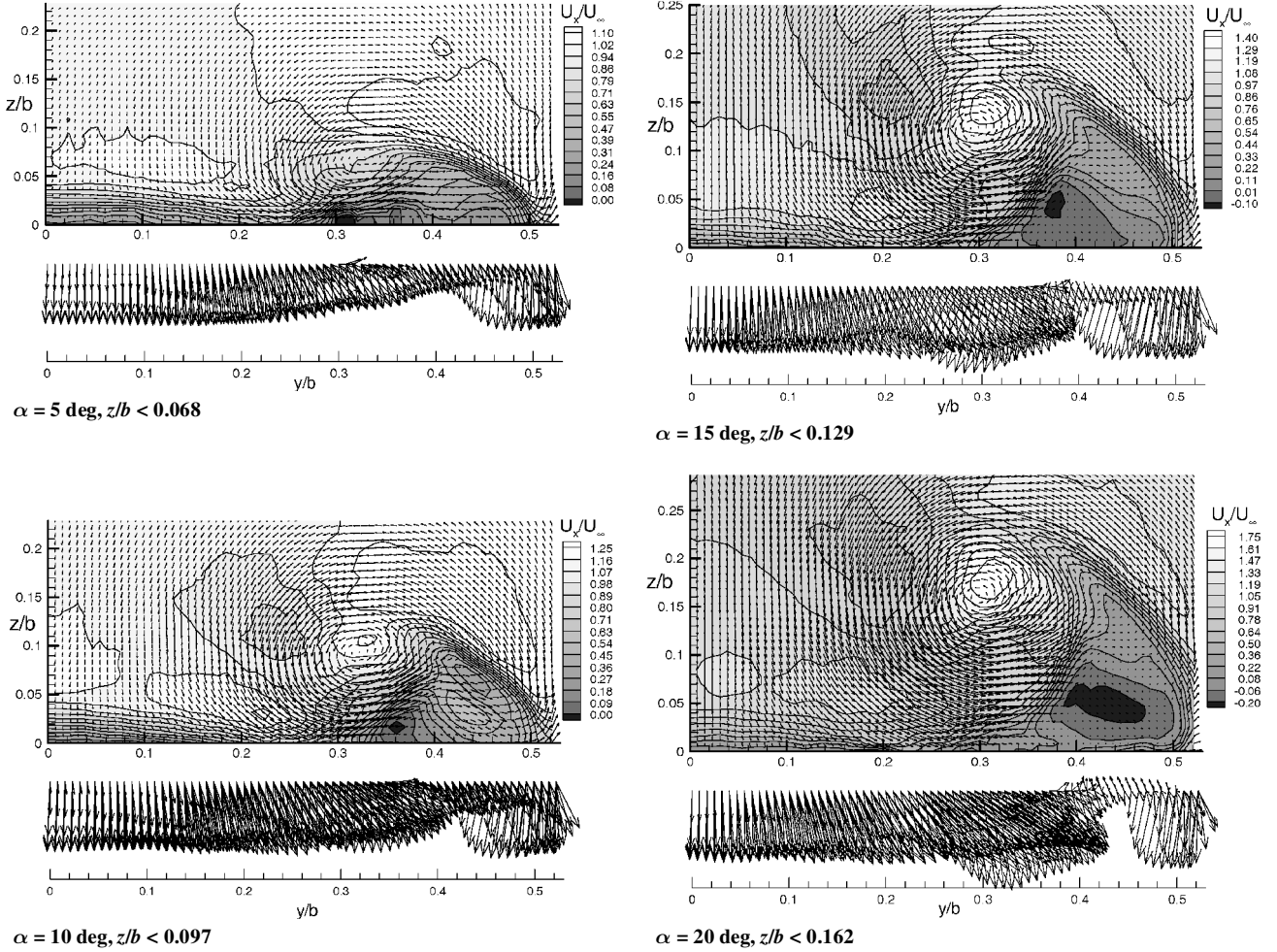
$\alpha = 5$ deg, $z/b < 0.068$

$\alpha = 15$ deg, $z/b < 0.129$

$\alpha = 10$ deg, $z/b < 0.097$

$\alpha = 20$ deg, $z/b < 0.162$

Fig. 9   Streamwise and planform views of the mean starboard flow pattern, 65-deg wing; $x/c = 0.296$; coordinates expressed in fractions of local span.

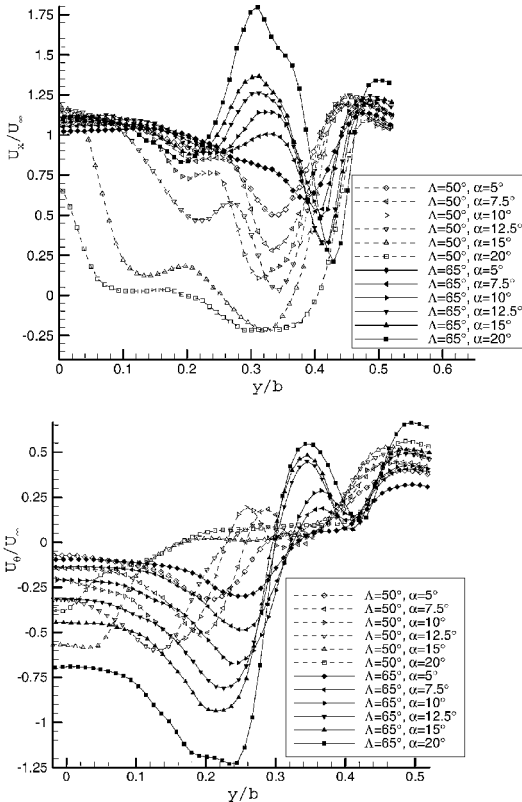
Fig. 10   Mean axial and azimuthal velocity profiles, 50- and 65-deg wings, $x/c = 0.296$.

could, thus, be used as a predictive criterion for incipient break-down of the primary LEV at slightly higher angles of attack. The near-stagnant flow outboard of the primary LEV is consistent with the low-Reynolds-number results of Traub[26] for wings of 60- and 70-deg sweep, at $Re = 2 \times 10^4$.

2.   Conical Flow Near the Apex

Here we consider axial and azimuthal velocity profiles of the $x/c = 0.118, 0.178, 0.237$, and 0.296 stations, for the 50-deg wing at 12.5- and 15-deg angles of attack. These are shown in Fig. 11. The abscissas for each x/c station were rescaled by the local semispan, so that the LE location for all curves is at $y/b = 0.5$. At each of the two angles of attack, the four velocity profiles are nearly coincident; that is, the velocity field exhibits a conical development, perhaps unexpectedly for a wing of 50-deg sweep.

3.   Observations at a Lower Reynolds Number

With the sole exception given in this section, all of the data in the present work were taken at a freestream flow speed of 80 mm/s. The following, however, were taken at 32 mm/s, corresponding to a Reynolds number of 6.2×10^3 based on root chord. This is the case of the 65-deg wing at $\alpha = 15$ deg.

Evidently, even when comparing one small Reynolds number to another, there are still important distinctions. In going from $Re = 1.54 \times 10^4$ to 6.2×10^3, the qualitative features of the primary LEV do not appear to have changed significantly[18]; this includes, for example, the location of the primary LEV core center. However, the velocity profiles, as seen in Fig. 12, are quite different. The higher Reynolds number case displays a relatively high LEV core axial velocity. The $Re = 6.2 \times 10^3$ case, however, has no discernable axial velocity peak in the LEV core. Perhaps paradoxically, the lower Reynolds number case reverses the supposed trend in increasingly
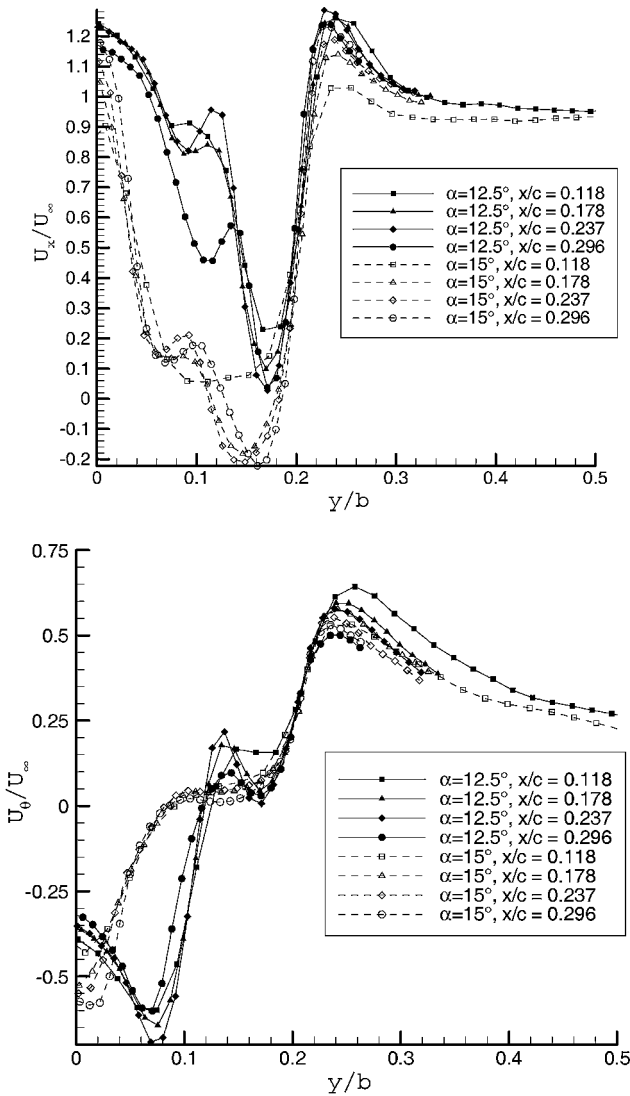
Fig. 12 Normalized 65-deg wing velocity profiles for two different Reynolds numbers, $x/c = 0.296$.

Fig. 11 Mean axial and azimuthal velocity profiles for the 50-deg wing, $\alpha = 12.5$ and 15 deg.
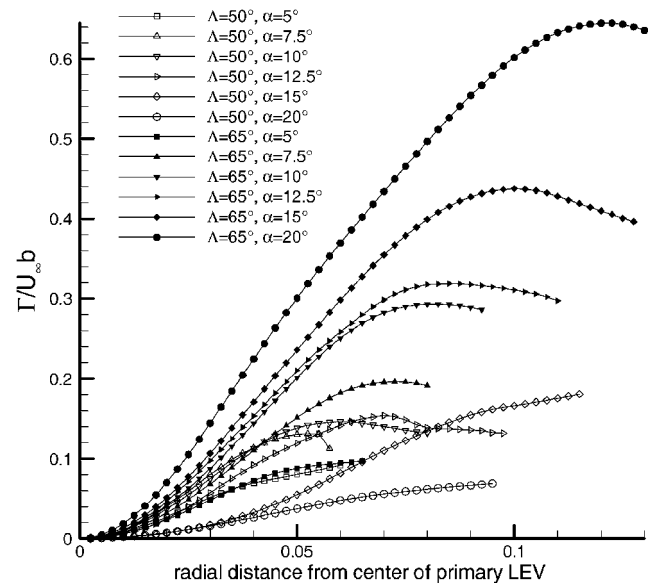
Fig. 13 Normalized circulation vs distance from LEV center.

more stagnant outboard flow going toward the lower Reynolds number.

The azimuthal velocity profile for the lower-Reynolds-number case is not broader than for the higher-Reynolds-number case, but shows lower variations and smaller gradients. Essentially, with a reduction in Reynolds number, the flowfield appears to be driven toward the state of an unperturbed freestream.

IV. Discussion

A. Circulation

Circulation can be computed from the velocity data by various means. A simple method is to take circular contours centered about some declared vortex core location and to compute the line integral of the tangential velocity component. Centering these circles about the primary LEV core location in the $x/c = 0.296$ crossflow plane and varying the radius of integration contours results in the data shown in Fig. 13. Data are given for the two wings and six angles of attack: $\alpha = 5, 7.5, 10, 12.5, 15,$ and 20 deg. The ordinate is circulation normalized by local span and the freestream velocity.

From Fig. 13, we can identify several trends:

1) In general, as the angle of attack is increased, the characteristic radius of the LEV (defined as the radius at which peak circulation is achieved) increases. This broadening of the LEV viscous core is especially clear for the 65-deg wing in going from 5 to 20-deg.

2) With increasing angle of attack for a given wing, circulation peak value also increases until breakdown approaches the cross-sectional station, where the circulation was measured.
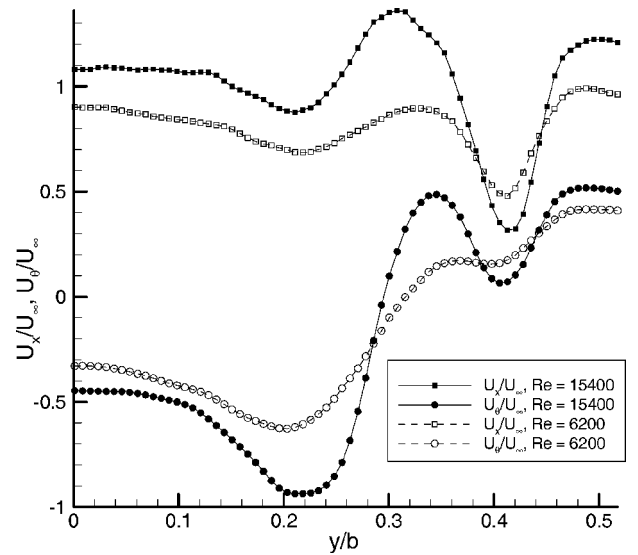
3) Peak circulation is lower in a postbreakdown situation. That is, if the angle of attack is increased to the point where breakdown crosses the station where the circulation was measured, that measurement will be lower than it was for the lower angle of attack when the vortex was in a prebreakdown condition.

4) For any given angle of attack, the LEVs of the 65-deg wing are both broader and stronger, that is, have more circulation, than those of the 50-deg wing.

5) Circulation curves for the two wings are similar at low angle of attack (almost identical at $\alpha = 5$ deg) and progressively differ more with increasing angle of attack, even for those angles at which breakdown was not observed.

The circulation curves for the 50-deg wing show convincing evidence that a breakdownlike condition crossed the $x/c = 0.296$ station somewhere between $\alpha = 12.5$ and 15 deg. The curve for the former angle has a definite circulation peak, whose size and radius follows the trend in going from the smaller angles of attack. The $\alpha = 15$-deg curve, however, shows no clear peak. The $\alpha = 20$-deg curve behaves similarly to the 15-deg curve, although the circulation magnitude is much lower.

Also note that, for the lower angles of attack, and especially for the 50-deg wing, the use of circular contours of integration for the
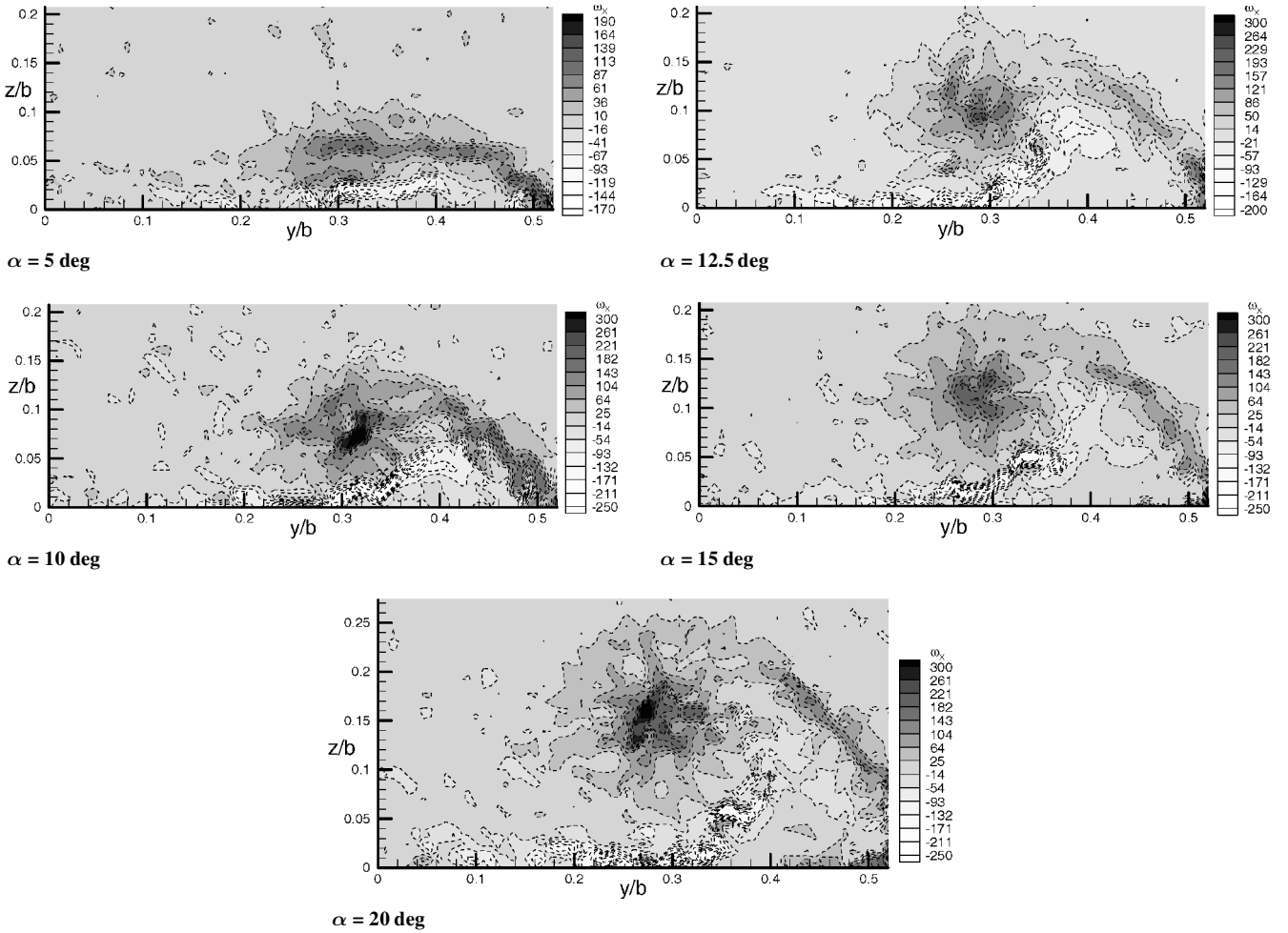
Fig. 14 Contours of instantaneous axial vorticity, 65-deg wing.

computation of vorticity might not be the best choice. Rotational structures for these cases tended to be more elliptical in cross-sectional shape, with the long axis of the ellipse in the spanwise direction.

That the peak circulation value is typically only attained at a radius comparable to the distance from the LEV center to the inner side of the LE shear layer is an indication that this entire region is viscosity dominated. In other words, at the Reynolds number of the present investigation, the "windings" of the shear layer can not be resolved into individual vortex sheets. The vorticity is diffused to the point where one can speak of the LEV core and the LEV itself almost interchangeably, at least in terms of the velocity components in crossflow planes.

The normalized axial velocity evaluated at the core radius that corresponds to the peak circulation was found to be rather smaller than 1.0. The classical result for delta wings is that the axial velocity at this radius should be comparable to freestream, or slightly greater.[27] The axial flow data for the 65-deg wing (Fig. 10), and especially for the 50-deg wing, are not symmetric about the core axis when taken at the radius of peak circulation.

B. Axial Vorticity Contours
Contours of instantaneous axial vorticity (that is, from one SPIV frame set) are given in the streamwise view for the 65-deg wing (Fig. 14) and the 50-deg wing (Fig. 15) for some representative cases. These data are instantaneous, rather than averages over some number of frames, in an effort to avoid temporal averaging of inter-mittently appearing vortical structures. The scope of these data is essentially identical to what one would have obtained from classical two-dimensional PIV. An extension to quasi-three-dimensional vor-ticity computation on the basis of generalized SPIV data obtained by central differencing across a triplet of interrogation planes is given

in Ref. 18. However, that approach is only possible for averaged vorticity data.

Whereas it is clear from the velocity vector plots (Figs. 8 and 9) that the primary LEV core will be a region of strong axial vorticity, at least in crossflow planes upstream of breakdown, small regions of concentrated vorticity (substructures), such as those observed by Shih and Ding,[7] Gad-el-Hak and Blackwelder,[28] and others, cannot be observed from the velocity plots alone. These were, however, clearly visible in the rolling-up shear layer and in the leeward surface boundary layer, especially where the latter is close to the primary LEV. The actual numerical values of vorticity are to be viewed with caution because peak vorticity values agglomerated from local errors (numerical noise, windowing resolution in region of high velocity gradients, etc.) in the PIV correlation-finding algorithm can strongly skew the entire image. Vorticity was computed from direct differentiation of cubic splines fitted to the velocity data.[29]

In going from $\alpha = 10$ to 12.5 to 15 deg, the strong axial vorticity in the primary core is dissipated. By $\alpha = 20$ deg, the region bounded by the rolled-up shear layer has no discernable vorticity peaks. In-terestingly, for the first time, the leading-edge shear layer displays strong vorticity substructures of both signs. This has implications for the balance of vorticity production and convection over the entire flowfield of the wing. If the LE shear layer contains counter-rotating structures, there is no longer the need to sustain a stable LEV as a downstream sink of vorticity, as would have been the case were the vorticity in the LE shear layer all of one sign.

All of the vorticity plots (Figs. 14 and 15), with the exception of those for the 50-deg wing at $\alpha = 15$ deg and especially $\alpha = 20$ deg, show at least a local axial vorticity peak in the general vicin-ity of the primary LEV core. A "slab" of vorticity of the opposite sign near the leeward boundary layer is also present, starting ap-proximately at the primary LEV attachment line and proceeding
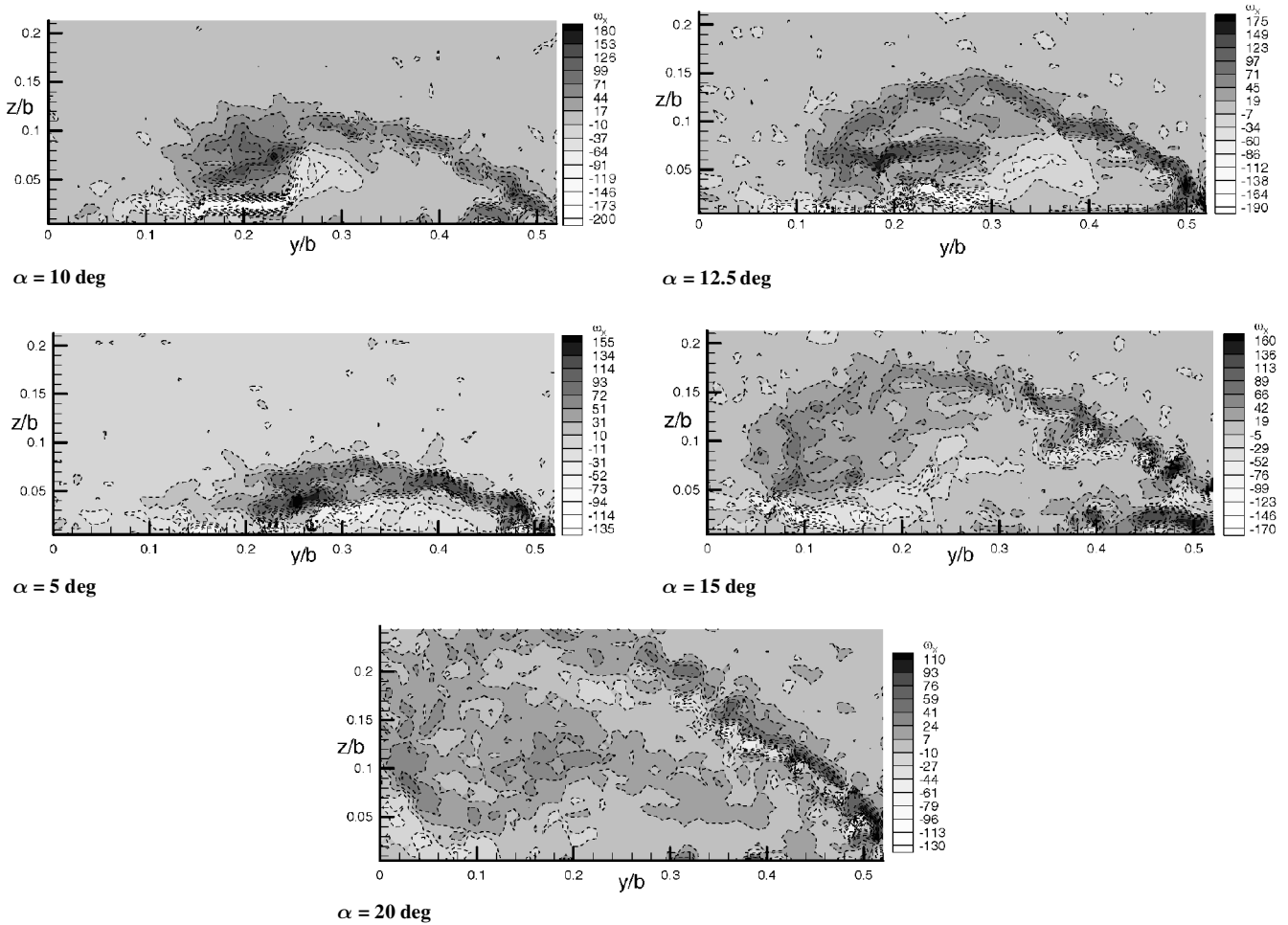
Fig. 15 Contours of instantaneous axial vorticity, 50-deg wing.

outboard. Again with the exception of the $\alpha = 20$-deg case, the substructures of instantaneous local vorticity peaks (in these particular instantaneous snapshots) in either family are mutually of the same sign and are not counter-rotating vortex pairs. The region between the boundary-layer vorticity slab and the LE shear layer is largely devoid of vorticity peaks, further supporting the assertion that this flow is essentially stagnant.

C. Vortex Core Trajectories

Geometry of the trajectory of the LEV, as evidenced by the location of the intersection of its core with a crossflow plane, is one of several possible measures of the distinction between a slender and nonslender delta wing. More important for the present investigation than the particular location of the LEV is the insight that measurements of the core location gives into 1) the applicability of theoretical models designed for slender delta wings and 2) the validity of the present data collection itself.

LEV core axis location can be identified from the stereo PIV data and the flow visualization data for the two wings and the various angles of attack considered in this study. Here, core refers not necessarily just to the viscous portion of the LEV structure, but to a hypothetical cylindrical tube of arbitrarily small cross section, centered about a curve defining the LEV trajectory. This curve is generally taken to be a straight line emanating from the wing apex. Indeed, in the flow visualizations, the dye streaks representative of this structure were nominally straight whenever a definable primary LEV was present, except for $\alpha = 5$ deg and below, where some curvature was observed.

Whereas the point where LEV trajectory intersects a given crossflow plane is obvious in the flow visualization if one identifies the dye streak with the LEV, in the PIV data one must assign some criterion to the velocity or vorticity field to identify the core. One option is to consider the location of the peak axial vorticity in the crossflow

plane. However, this criterion can be ambiguous when a vorticity peak is poorly defined, as is especially the case for the 50-deg wing above 12.5-deg angle of attack. The alternative common criterion of peak axial velocity fails even more dramatically, in light of the axial velocity deficit in the 50-deg LEVs. Instead, the LEV core centers were deduced from plots of crossflow-plane projected streamlines. Although these projections can not, in general, be identified with actual streamlines, they do help to identify singular points in the flow topology.[30] Collapsing the SPIV data to the two planar velocity components results in two-dimensional data sets to which fictitious streamlines can be drawn. In all cases, these lines would wind about the general vicinity of the primary LEV core in nearly circular curves, resembling closed streamlines or limit cycles. The center of such a closed curve was then taken to be the LEV core location in that crossflow plane. Spanwise locations in the crossflow plane $x/c = 0.296$ of points corresponding to this definition of LEV core axis are shown in Fig. 16. Flow visualization and SPIV data are plotted together, where both data are available for a particular angle of attack with the angle of attack labeled. The abscissa in Fig. 16, a, is a similarity parameter that combines sweep angle and angle of attack. First proposed for slender delta wings by Smith,[31] it can be written as $a = \tan\alpha/[\tan(\pi/2 - \Lambda)]$. Were the flow to be conical in the sense of Smith's result, data for the different sweeps and angles of attack would collapse onto the same point if the parameter a were the same. Smith's prediction gives values of core spanwise location that are rather far outboard of those of the present data set. As expected, the data for the 65-deg wing fit the model much better than do the 50-deg wing data. In particular, the former have a slope vs a comparable to the model's prediction. Note that Smith's model assumes the existence of discrete windings of the LE vortex sheet, wherein the vortex sheet winds about the LEV core axis for many revolutions before finally spiraling into a thin core. This assumption is consistent with Reynolds number approaching infinity
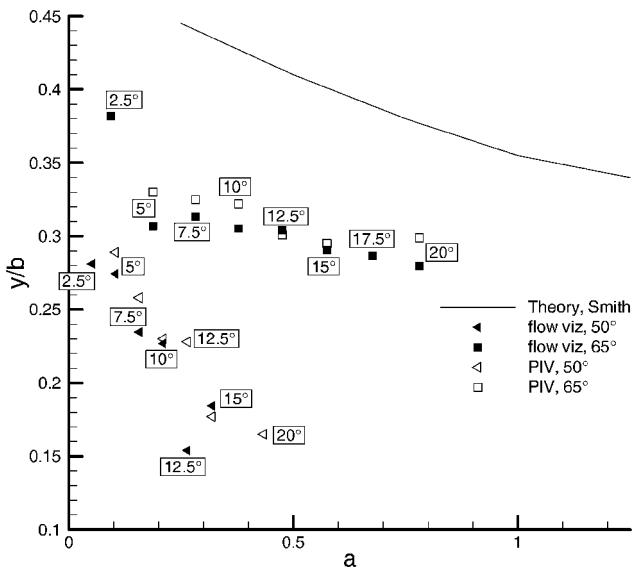
Fig. 16   LEV core spanwise location for 50- and 65-deg wings measured at $x/c = 0.296$.

and, not surprisingly, contradicts the conjecture of the present work; namely, that the LE shear layer makes at most a single revolution before being subsumed in a smeared, viscous rotating flow.

We note that with the exception of the highly unsteady case of the 50-deg wing at $\alpha = 12.5$ deg, the flow visualization and SPIV data match fairly closely. It is seen that, for the 65-deg wing, the spanwise location of the cores is remarkably constant for all angles of attack except 2.5 deg, whereas for the 50-deg wing, the cores move appreciably inboard with increasing angle of attack. This behavior for the 65-deg wing, but not the 50-deg wing, is consistent with the recent inviscid theory of Moore and Pullin[32] for nonslender delta wings. Their conclusion, which departs from the result of slender-body theory, is that the (primary) LEV core location should not vary with angle of attack for a semi-infinite delta wing of arbitrary sweep. In some sense, this should be applicable to the near-apex region of a real, finite wing. The result of the present experiments is that the primary LEV spanwise location indeed varies little in going across the angle of attack range of 5–20 deg, although the LEV vertical location above the wing leeward surface does increase appreciably.

V.   Conclusions

The present study attempts to describe the near-apex flowfield of a slender and a nonslender delta wing with quasi-three-dimensional data obtainable by SPIV. As the LE sweep angle of a delta wing becomes progressively lower, one can intuitively expect the flowfield to behave less like that of a slender delta wing and more akin to that of a classical unswept wing. In particular, this should be reflected in the nature of the wing's LE separation and separated vortex rollup and whether such separation can be identified with a stall-like condition distinct from the usual upstream progression of vortex breakdown with increasing angle of attack for slender delta wings.

At low angles of attack (10 deg and below) the candidate non-slender wing of 50-deg LE sweep had a similar flowfield to that of the 65-deg wing; that is, the geometry of the LE shear layer, the presence of a primary LE vortex, and the axial velocity distribution were similar. Likewise, the gradual upstream progression of the vortex breakdown location with increasing angle of attack was similar, as long as the angle of attack was below 10 deg. However, at higher angles of attack, the two flowfields diverge even qualitatively, not merely because the lower-sweep wing experiences breakdown at lower angle of attack, but, more importantly, because of a large-scale collapse of the rolled-up LEV structure in going across a narrow angle of attack range for the 50-deg wing. With increasing angle of attack, the more slender delta wing exhibits the usual jetlike axial velocity profile of stable primary LE vortices, whereas

the 50-deg wing fails to have a significant axial velocity peak even for conditions devoid of identifiable vortex breakdown.

The effect of low Reynolds number is, of course, to increase the role of viscosity. This is evidenced in very broad primary LEV cores and in the curious attenuation of secondary separation beginning at $\alpha = 10$ deg. At higher angles of attack, the flow in this region tends to stagnate or even reverse streamwise direction. It remains to be seen, first, what conditions would be observed at yet lower Reynolds numbers and, second, how the velocity profiles transition into the more usually observed patterns at the higher Reynolds numbers.

References

[1]Jones, R. T., "Wing Plan Forms for High-Speed Flight," NACA Rept. 863, 1947.

[2]Polhamus, E. C., "Vortex Lift Research: Early Contributions and Some Current Challenges," *Vortex Flow Aerodynamics*, Vol. 1, NASA CP-2416, 1985, pp. 1–30.

[3]Kuechemann, D., *The Aerodynamic Design of Aircraft*, Pergamon, New York, 1978.

[4]Mangler, K. W., and Smith, J. H. B., "A Theory of the Flow Past a Slender Delta Wing with Leading-Edge Separation," *Proceedings of the Royal Society of London, Series A: Mathematical and Physical Sciences*, Vol. 251, 1959, pp. 200–217.

[5]Hummel, D., "On the Vortex Formation over a Slender Wing at Large Angles of Incidence," *High Angle of Attack Aerodynamics*, CP-247, AGARD, 1979, pp. 15-1–15-17.

[6]Ayoub, A., and McLachlan, B. G., "Slender Delta Wing at High Angles of Attack—A Flow Visualization Study," AIAA Paper 87-1230, June 1987.

[7]Shih, C., and Ding, Z., "Unsteady Structure of Leading-Edge Vortex Flow over a Delta Wing," AIAA Paper 96-0664, Jan. 1996.

[8]Rockwell, D., "Three-Dimensional Flow Structure on Delta Wings at High Angle-of-Attack: Experimental Concepts and Issues," AIAA Paper 93-0550, Jan. 1993.

[9]Payne, F. M., Ng, T. T., and Nelson, R. C., "Experimental Study of the Velocity Field on a Delta Wing," AIAA Paper 87-1231, June 1987.

[10]Wentz, W. H., and Kohlman, D. L., "Vortex Breakdown on Slender Sharp-Edged Wings." *Journal of Aircraft*, Vol. 8, No. 3, 1971, pp. 156–161.

[11]Nelson, R. C., and Pelletier, A., "An Experimental Investigation of Vortex Breakdown on Slender Delta-Wing Planforms," Dept. of Aerospace and Mechanical Engineering, Univ. of Notre Dame, Contractor Rept., Notre Dame, IN, Aug. 1994.

[12]Honken, A., and Andreopoulos, J., "Instantaneous Three-Dimensional Vorticity Measurements in a Vortical Flow over a Delta Wing," AIAA Paper 95-0587, Jan. 1995.

[13]Earnshaw, P. B., and Lawford, J. A., "Low-Speed Wind Tunnel Experiments on a Series of Sharp-Edged Delta Wings," Repts. and Memorabilia, No. 3424, March 1964, pp. 1–47.

[14]Miau, J. J., Kuo, K. T., Liu, W. H., Hsieh, S. J., Chou, J. H., and Lin, C. K., "Flow Developments Above 50-Degree Sweep Delta Wings with Different Leading-Edge Profiles," *Journal of Aircraft*, Vol. 32, No. 4, 1995, pp. 787–796.

[15]Kegelman, J. T., and Roos, F. W., "Effects of Leading Edge Shape and Vortex Burst on the Flowfield of a 70-Degree-Sweep Delta Wing," AIAA Paper 89-0086, Jan. 1989.

[16]Willert, C. E., "Stereoscopic Digital Particle Image Velocimetry for Application in Wind Tunnel Flows," *Measurement Science Technology*, Vol. 8, No. 12, 1997, pp. 1465–1479.

[17]Ol, M., "The Passage Toward Stall of Nonslender Delta Wings at Low Reynolds Number," AIAA Paper 2001-2843, June 2001.

[18]Ol, M., "The Passage Toward Stall of Nonslender Delta Wings at Low Reynolds Number," Ph.D. Dissertation, Dept. of Aeronautics, California Inst. of Technology, Pasadena, CA, Dec. 2000.

[19]Jobe, C. E., "Vortex Breakdown Location over 65-Degree Delta Wings—Empiricism and Experiment," AIAA Paper 98-2526, June 1998.

[20]Willert, C. E., and Gharib, M., "Digital Particle Image Velocimetry," *Experiments in Fluids*, Vol. 10, 1991, pp. 181–193.

[21]Lawson, N. J., and Wu, J., "Three-Dimensional Particle Image Velocimetry: Experimental Error of a Digital Angular Stereoscopic System," *Measurement Science Technology*, Vol. 8, No. 8, 1997, pp. 894–900.

[22]Lab. for Experimental Fluid Dynamics, Johns Hopkins Univ., Baltimore, MD, URL: http://www.me.jhu.edu/~lefd/particles.htm.

[23]Soloff, S. M., Adrian, R. J., and Liu, Z.-C., "Distortion Compensation for Generalized Stereoscopic Particle Image Velocimetry," *Measurement Science Technology*, Vol. 8, No. 12, 1997, pp. 1441–1454.

[24]Westerweel, J., Dabiri, D., and Gharib, M., "The Effect of Discrete Window Offset on the Accuracy of Cross-Correlation Analysis of Digital PIV Recordings," *Experiments in Fluids*, Vol. 23, No. 1, 1997, pp. 20–28.

[25]Ol, M., "An Experimental Investigation of Leading Edge Vortices and Passage to Stall of Nonslender Delta Wings," Symposium on Advanced Flow Management, RTO AVT-072, May 2001, Paper 2.

[26]Traub, L., "Low-Reynolds-Number Effects on Delta Wing Aerodynamics," *Journal of Aircraft*, Vol. 35, No. 4, 1998, pp. 653–656.

[27]Hall, M. G., "A Theory for the Core of a Leading-Edge Vortex," *Journal of Fluid Mechanics*, Vol. 11, 1961, pp. 209–228.

[28]Gad-el-Haq, M., and Blackwelder, R. F., "The Discrete Vortices from a Delta Wing," *AIAA Journal*, Vol. 23, No. 6, 1985, pp. 961, 962.

[29]Jeon, D., "On Cylinders Undergoing One- and Two-Degree of Freedom Forced Vibrations in a Steady Flow," Ph.D. Dissertation, Dept. of Aeronautics, California Inst. of Technology, Pasadena, CA, May 2000.

[30]Delery, J. M., "Aspects of Vortex Breakdown," *Progress in Aerospace Sciences*, Vol. 30, No. 1, 1994, pp. 1–59.

[31]Smith, J. H. B., "Improved Calculations of Leading Edge Separation from Slender, Thin Delta Wings," *Proceedings of the Royal Society of London, Series A: Mathematical and Physical Sciences*, Vol. A 306, 1968, pp. 67–90.

[32]Moore, D. W., and Pullin, D. I., "Inviscid Separated Flow over a Non-Slender Delta Wing," *Journal of Fluid Mechanics*, Vol. 305, 1995, pp. 307–345.

A. Plotkin
Associate Editor